HAL
open science

Assessment of two Harmonic Balance Method-based numerical strategies for blade-tip/casing interactions: application to NASA rotor67

Thibaut Vadcard, Yann Colaïtis, Alain Batailly, Fabrice Thouverez

To cite this version:

Thibaut Vadcard, Yann Colaïtis, Alain Batailly, Fabrice Thouverez. Assessment of two Harmonic Balance Method-based numerical strategies for blade-tip/casing interactions: application to NASA rotor67. ASME Turbo Expo 2022 Turbomachinery Technical Conference and Exposition 2022, Jun 2022, Rotterdam, Netherlands. 10.1115/GT2022-81694 . hal-03775624

HAL Id: hal-03775624

https://hal.science/hal-03775624v1

Submitted on 12 Sep 2022

HAL is a multi-disciplinary open access archive for the deposit and dissemination of scientific research documents, whether they are published or not. The documents may come from teaching and research institutions in France or abroad, or from public or private research centers.

L'archive ouverte pluridisciplinaire **HAL**, est destinée au dépôt et à la diffusion de documents scientifiques de niveau recherche, publiés ou non, émanant des établissements d'enseignement et de recherche français ou étrangers, des laboratoires publics ou privés.

POLYTECHNIQUE MONTRÉAL
UNIVERSITÉ D'INGÉNIERIE

LABORATOIRE D'ANALYSE VIBRATOIRE ET ACOUSTIQUE

Assessment of two Harmonic Balance Method-based numerical strategies for blade-tip/casing interactions: application to NASA rotor67

T. Vadcard[1,2], Y. Colaïtis[1], A. Batailly[1], F. Thouverez[2]

Abstract

The study presented in this paper focuses on the analysis of rubbing interactions —including unilateral contact and dry friction— between a rotating fan blade and a rigid casing by frequency domain methods. Two previously published Harmonic Balance Method-based methodologies are assessed: 1) an approach relying on augmented lagrangians and 2) a second method using a regularized penalty law combined with a Lanczos σ-approximation filter. As a reference point for this comparison, a time-domain numerical strategy relying on a Lagrange multiplier-based contact treatment is considered. All computations are run with the NASA rotor 67 fan blade, an open industrial blade geometry. As it undergoes structural contacts, this blade features an intricate dynamics response, thus making it a challenging case study for nonlinear iterative solvers. The contact scenario is chosen to be an ovalization of the casing with no external forcing. This scenario induces highly nonlinear reponses of the blade and complex phenomena such as isolated frequency response curves. The results presented underline a very good agreement of the different strategies with the reference time marching approach. An in-depth comparison is made with an emphasis on nonlinear frequency response curves and time signals. Finally, a physical analysis of the encountered isolas is presented through an in-depth investigation of the main modal contributions for each computed solution. In the end, this paper provides new qualitative elements allowing for a better understanding of rubbing interactions that may not be efficiently obtained with time marching procedures.

Keywords

Harmonic Balance Method, unilateral contact, rotor/stator interaction, fan blade, isola

1 - Département de génie mécanique, École Polytechnique de Montréal, P.O. Box 6079, Succ. Centre-Ville, Montréal, Québec, Canada H3C 3A7
2 - École Centrale de Lyon, Laboratoire de Tribologie et Dynamique des Systèmes, UMR CNRS 5513, 36 avenue Guy de Collongue, Écully, 69134, France

Évaluation de deux stratégies numériques basées sur la méthode de l'équilibrage harmonique pour les interactions aube/carter : application au NASA rotor 67

T. Vadcard[1,2], Y. Colaïtis[1], A. Batailly[1], F. Thouverez[2]

Résumé

L'étude présentée dans ce papier se focalise sur l'analyse des contacts frottants aube/carter—incluants contact unilatéral et frottement sec—entre une aube de soufflante en rotation et un carter rigide par des méthodes fréquentielles. Deux méthodes précedemment publiées basées sur la méthode d'équilibrage harmonique sont évaluées : 1) une approche se basant sur des lagrangiens augmentés et 2) une deuxième méthode utilisant une loi de pénalité régularisée combinée avec un filtre à σ-approximation de Lanczos. Une méthode numérique du domaine temporel basée sur un traitement du contact par multiplicateurs de Lagrange est considérée comme point de référence pour la comparaison. Tous les calculs sont réalisés avec l'aube de soufflante du NASA rotor 67, une géometrie d'aube industrielle ouverte. Lorsqu'elle subit des contact structurels, cette aube présente une réponse dynamique complexe, en faisant un cas d'application difficile à traiter par des solveurs non-linéaires itératifs. Le scénario de contact choisi est une ovalisation du carter avec aucun forçage extérieur. Ce scénario entraîne une réponse hautement non-linéaire et des phénomènes complexes tels que des branches de solutions isolées. Les résulats présentés soulignent un très bon accord entre les différentes stratégies et la méthode de référence du domaine temporel. Une comparaison approfondie est faite en mettant l'emphase sur les courbes de réponse en fréquence et les signaux temporels. Finalement, une étude physique des isolats rencontrés est conduite à travers une enquête approfondie sur les contributions mdoales principales pour chacune des solutions calculées. En conclusion, ce papier fournit de nouveaux éléments qualitatifs permettant une meilleur compréhension des interactions de contacts frottants aube/carter qui ne pourraient pas être obtenus par l'usage de méthodes du domaine temporel.

Mots-clés

Méthode d'équilibrage harmonique, contact unilatéral, interaction aube/carter, aube de soufflante, isolat

1 - Département de génie mécanique, École Polytechnique de Montréal, P.O. Box 6079, Succ. Centre-Ville, Montréal, Québec, Canada H3C 3A7
2 - École Centrale de Lyon, Laboratoire de Tribologie et Dynamique des Systèmes, UMR CNRS 5513, 36 avenue Guy de Collongue, Écully, 69134, France

INTRODUCTION

With the recent evolution of environmental regulations for commercial aviation, aircraft engine manufacturers are commited to designing more efficient turbomachines. Among the avenues considered to lower aircraft engines' environemental footprint, the reduction of operating tip clearances yields a significant gain in performance by decreasing parasitic leakage flows. However, this design choice yields new challenges for designers particularly because phenomena that were once considered as purely accidental now occur within nominal operating conditions. Among these critical phenomena, blade-tip/casing structural contacts are of particular interest [1, 2, 3, 4, 5, 6, 7, 8, 9, 10]. Since these situations are now expected in non-accidental configurations during the lifetime of engines, they must be accounted for in the design phase.

Full-scale experimental setups for blade/casing contact interactions are extremely costly. Hence, the developpement of predictive numerical strategies in order to accurately describe these interactions is an active field of research [11, 12, 13, 14]. To this day, the industrial state-of-the-art strategies are based on the time domain paradigm [3, 15, 16]. However, the development of methods relying on the frequency domain has known a renewed interest [9, 10, 14, 17, 18, 19]. Indeed, such methods have the potential to provide a qualitative understanding of a blade's response that would be extremely costly to get with time domain solution methods.

The present article focuses on the assessment of two previously published Harmonic Balance Method (HBM)-based strategies to evaluate nonlinear contact forces in a blade-tip/casing interaction configuration: on the one hand, the recently proposed Regularized-Lanczos HBM [14] and on the other hand the Dynamic Lagrangian Frequency Time HBM [20], an industrial standard for the characterization of friction damping for blade/disk assemblies. These two methodologies mainly differ by the way contact constraints are numerically handled.

Both Harmonic Balance (HB) methods are applied in a highly nonlinear configuration in order to validate the robustness of the strategies. The sophisticated responses also exacerbate modeling differences thus highlighting the specificities of each algorithm. The second section Sec. 1 focuses on presenting the classical HB approach, the specific developpements of each contact model, as well as the blade model and the contact scenario. The third section Sec. 2 presents a detailed comparison of the HB strategies with each other and the time-marching reference algorithm. The in-depth comparison covers: nonlinear frequency response curves, sophisticated isolated frequency response curves uncovered by frequency sweeps and time signals associated with some harmonic solutions as a validation. Finally, a specific isola is analyzed in terms of both modal and harmonic contributions to better underline the intricacy of the blade's dynamics.

1 HARMONIC BALANCE METHODOLOGIES

The time and space-normalized nonlinear equation of motion for a n-dof (degrees of freedom) system with respect to time reads:

$$\frac{\alpha}{\beta^2}\mathbf{M}\ddot{\mathbf{x}}(t) + \frac{\alpha}{\beta}\mathbf{C}\dot{\mathbf{x}}(t) + \alpha\mathbf{K}\mathbf{x}(t) + \mathbf{f}_{\mathrm{nl}}(\mathbf{x}(t), \dot{\mathbf{x}}(t), \omega) = \mathbf{0} \tag{1}$$

where $\mathbf{x}$ is the unknown displacement field, $\mathbf{M}$, $\mathbf{C}$ and $\mathbf{K}$ respectively stand for the mass, damping and stiffness matrices, $\mathbf{f}_{\mathrm{nl}}$ is the nonlinear forces vector and ω the fundamental pulsation of the contact forces. The overdots refer to time derivatives. Since no external forces are considered in this study, the related term is ommited in the equations. The time and space quantities are normalized thanks to the terms α and β chosen beforehand such that $\|\alpha\mathbf{x}\| \simeq 1$ and $\frac{\omega}{\beta} \simeq 1$ on the whole frequency range, this normalization yields a significant improvement in the overall numerical performance and convergence of the nonlinear iterative solvers.

1.1 Harmonic balance method

The HBM relies on the assumption that the displacement field solution to (1) can be expressed as a N_{h}-truncated Fourier series of fundamental pulsation ω.

$$\mathbf{x}(t) \simeq \frac{1}{2}\mathbf{a}_0 + \sum_{k=1}^{N_{\mathrm{h}}} \left(\mathbf{a}_k \cos(k\omega t) + \mathbf{b}_k \sin(k\omega t)\right) \tag{2}$$

where the vectorial quantities $\mathbf{a}_k$ and $\mathbf{b}_k$ are the real Fourier coefficients. These vectors of size n are organized such that,

$$\begin{cases} \mathbf{a}_k = [a_k^1, a_k^2, \dots, a_k^n] \text{ for } k \in [\![0, N_\mathrm{h}]\!] & (3) \\ \mathbf{b}_k = [b_k^1, b_k^2, \dots, b_k^n\ ] \text{ for } k \in [\![1, N_\mathrm{h}]\!] & (4) \end{cases}$$

The same harmonic decomposition is used to express the nonlinear forces $\mathbf{f}_\mathrm{nl}(\mathbf{x}(t), \dot{\mathbf{x}}(t), \omega)$. Fourier coefficients are gathered in the so called multiharmonic vectors of dimension $n(2N_\mathrm{h}+1)$, as written in (5).

$$\begin{aligned} \widetilde{\mathbf{x}} &= \left[\frac{1}{2}\mathbf{a}_0,\ \mathbf{a}_1,\ \mathbf{b}_1, \dots\ \mathbf{a}_{N_\mathrm{h}},\ \mathbf{b}_{N_\mathrm{h}}\right]^\top \\ \widetilde{\mathbf{f}}_\mathrm{nl} &= \left[\frac{1}{2}\mathbf{a}_0^\mathrm{nl},\ \mathbf{a}_1^\mathrm{nl},\ \mathbf{b}_1^\mathrm{nl}, \dots,\ \mathbf{a}_{N_\mathrm{h}}^\mathrm{nl},\ \mathbf{b}_{N_\mathrm{h}}^\mathrm{nl}\right]^\top \end{aligned} \tag{5}$$

By substituting the new expressions of the displacement vector given in (2), its derivatives, $\dot{\mathbf{x}}(t)$ and $\ddot{\mathbf{x}}(t)$, and the nonlinear forces in the differential equation of motion (1), it is possible to apply a Fourier-Galerkin projection yielding the $n(2N_\mathrm{h}+1)$ nonlinear algebraeic equations (6) where $\widetilde{\mathbf{x}}$ is the new unknown.

$$\mathbf{H}(\widetilde{\mathbf{x}}, \omega) = \mathbf{Z}(\omega)\widetilde{\mathbf{x}} + \widetilde{\mathbf{f}}_\mathrm{nl}(\widetilde{\mathbf{x}}) = \mathbf{0} \tag{6}$$

with $\mathbf{Z}(\omega)$ is the dynamic stiffness matrix, accounting for the linear behaviour of the structure. The matrix $\mathbf{Z}(\omega)$ is block diagonal and its blocks $\mathbf{Z}_k \forall k \in [\![0, N_\mathrm{h}]\!]$ are expressed as,

$$\mathbf{Z}_0 = \alpha\mathbf{K}, \quad \mathbf{Z}_k(\omega) = \alpha \begin{pmatrix} \mathbf{K} - \left(\dfrac{k\omega}{\beta}\right)^2 \mathbf{M} & \dfrac{k\omega}{\beta}\mathbf{C} \\ -\dfrac{k\omega}{\beta}\mathbf{C} & \mathbf{K} - \left(\dfrac{k\omega}{\beta}\right)^2 \mathbf{M} \end{pmatrix} \tag{7}$$

In order to reduce the size of the nonlinear system, an exact condensation on the nonlinear dof is conducted on the frequency domain nonlinear system (6). This strategy is commonly used on localized nonlinearities such as contact interactions and detailed in [14]. It relies on the property that linear dof do not withstand nonlinear forces by definition. The subscript $\bullet_\mathrm{r}$ refers to this condensation in further equations, such that the condensed equation of motion in the frequency domain reads:

$$\mathbf{H}_\mathrm{r}(\widetilde{\mathbf{x}}_\mathrm{r}, \omega) = \mathbf{Z}_\mathrm{r}(\omega)\widetilde{\mathbf{x}}_\mathrm{r} + \widetilde{\mathbf{f}}_\mathrm{nl,r}(\widetilde{\mathbf{x}}_\mathrm{r}) = \mathbf{0} \tag{8}$$

1.2 Iterative resolution

The HBM system (8) is nonlinear due to nonlinear forces that nontrivially depend on the displacement field $\widetilde{\mathbf{x}}_\mathrm{r}$. It is then necessary to use dedicated algorithms in order to find solutions to this system, such as the Newton-Raphson algorithm. This method computes iteratively a solution to the nonlinear equations, starting from an initial iterate $\widetilde{\mathbf{x}}_\mathrm{r}^0$. The methodology relies on the following iterative step:

$$\widetilde{\mathbf{x}}_\mathrm{r}^{k+1} = \widetilde{\mathbf{x}}_\mathrm{r}^k + \Delta\widetilde{\mathbf{x}}_\mathrm{r}^k \text{ where } \frac{\partial \mathbf{H}_\mathrm{r}}{\partial \widetilde{\mathbf{x}}_\mathrm{r}}(\widetilde{\mathbf{x}}_\mathrm{r}^k, \omega)\Delta\widetilde{\mathbf{x}}_\mathrm{r}^k = -\mathbf{H}_\mathrm{r}(\widetilde{\mathbf{x}}_\mathrm{r}^k, \omega) \tag{9}$$

In order to use this procedure, it is necessary to compute the jacobian matrix $\dfrac{\partial \mathbf{H}_\mathrm{r}}{\partial \widetilde{\mathbf{x}}_\mathrm{r}}(\widetilde{\mathbf{x}}_\mathrm{r}^k, \omega)$ at every step, its expression reads:

$$\frac{\partial \mathbf{H}_\mathrm{r}}{\partial \widetilde{\mathbf{x}}_\mathrm{r}}(\widetilde{\mathbf{x}}_\mathrm{r}^k, \omega) = \mathbf{Z}_\mathrm{r}(\omega) + \frac{\partial \widetilde{\mathbf{f}}_\mathrm{nl,r}}{\partial \widetilde{\mathbf{x}}_\mathrm{r}}(\widetilde{\mathbf{x}}_\mathrm{r}^k, \omega) \tag{10}$$

Once the objective function $\|\mathbf{H}_\mathrm{r}(\widetilde{\mathbf{x}}_\mathrm{r},\omega)\|_2$ has reached a sufficiently low value, a solution has been found and the iterations stop.

The presence of nonlinear forces in the frequency domain leads to specific numerical challenges. In fact, the laws governing nonlinear forces are usually tailored for time domain strategies. For the case of contact forces, it is even more challenging since no explicit expression exists nor for the Hertz-Signorini-Moreau conditions or the Coulomb's law. In order to model such nonlinear phenomena, one has to use dedicated strategies for the evaluation of the contact forces. Two methodologies are proposed in this paper for this purpose, the first one is based on the augmented lagrangian formalism and the second one relies a regularized penalty law associated with a Lanczos σ-approximation filter. Each of these strategies are thoroughly presented in Sec. 1.4 and Sec. 1.5. Both methods rely on the Alternating Frequency/Time (AFT) scheme that is explicited in Sec. 1.3.

1.3 Alternating frequency/time strategy

Since the governing laws related to the nonlinear forces can solely be expressed in the time domain, dedicated methodologies are required in order to deal with nonlinear forces in the frequency domain. As suggested in [21], the AFT scheme allows to evaluate nonlinear forces and their derivatives for each iteration of the Newton-Raphson algorithm. This strategy requires the choice of a time discretization beforehand: the period is chosen to be divided in N_t evenly spaced time instants. The AFT method is usually divided in three main steps: 1) the Inverse Discrete Fourier Transform (IDFT) on the multiharmonic vector $\widetilde{\mathbf{x}}_\mathrm{r}$ in order to obtain the time-discrete vector $\{\mathbf{x}_\mathrm{r}(t_i)\}_{i=1\ldots N_\mathrm{t}}$, 2) the evaluation of the time-discrete vector of nonlinear forces $\{\mathbf{f}_\mathrm{nl,r}(t_i)\}_{i=1\ldots N_\mathrm{t}}$ using a methodology dedicated to the type of nonlinearity, and 3) the Discrete Fourier Transform (DFT) to compute the multiharmonic vector of nonlinear forces $\widetilde{\mathbf{f}}_\mathrm{nl,r}$ and then evaluate the objective function $\mathbf{H}_\mathrm{r}(\widetilde{\mathbf{x}}_\mathrm{r},\omega)$. The first and last steps are realized by using the IDFT matrix $\overline{\mathbf{F}}$ and DFT matrix $\mathbf{F}$, expressed as follows:

$$\overline{\mathbf{F}} = \begin{pmatrix} \frac{1}{2} & \cos(\omega t_1) & \sin(\omega t_1) & \ldots & \cos(N_\mathrm{h}\omega t_1) & \sin(N_\mathrm{h}\omega t_1) \\ \vdots & \vdots & \vdots & & \vdots & \vdots \\ \frac{1}{2} & \cos(\omega t_{N_\mathrm{t}}) & \sin(\omega t_{N_\mathrm{t}}) & \ldots & \cos(N_\mathrm{h}\omega t_{N_\mathrm{t}}) & \sin(N_\mathrm{h}\omega t_{N_\mathrm{t}}) \end{pmatrix} \otimes \mathbf{I}_n \tag{11}$$

$$\mathbf{F} = \frac{2}{N_\mathrm{t}} \begin{pmatrix} 1 & \ldots & 1 \\ \cos(\omega t_1) & \ldots & \cos(\omega t_{N_\mathrm{t}}) \\ \sin(\omega t_1) & \ldots & \sin(\omega t_{N_\mathrm{t}}) \\ \vdots & & \vdots \\ \cos(N_\mathrm{h}\omega t_1) & \ldots & \cos(N_\mathrm{h}\omega t_{N_\mathrm{t}}) \\ \sin(N_\mathrm{h}\omega t_1) & \ldots & \sin(N_\mathrm{h}\omega t_{N_\mathrm{t}}) \end{pmatrix} \otimes \mathbf{I}_n \tag{12}$$

These matrices allow to transfer any quantity $\bullet(t)$ from the time domain to the frequency domain $\widetilde{\bullet}$ ($\mathbf{F}$) or vice-versa ($\overline{\mathbf{F}}$), as represented in (13).

$$\widetilde{\bullet} = \mathbf{F}\,\{\bullet(t_i)\}_{i=1\ldots N_\mathrm{t}} \qquad \{\bullet(t_i)\}_{i=1\ldots N_\mathrm{t}} = \overline{\mathbf{F}}\widetilde{\bullet} \tag{13}$$

This methodology is very efficient when it comes to nonlinearities that can be written as analytical expressions. However, in the case of contact a direct use of the AFT is not possible since no analytical expression links the displacement field $\mathbf{x}_\mathrm{r}(t)$ to the nonlinear forces $\mathbf{f}_\mathrm{nl,r}(t)$. In this paper, two very different approaches are given in Sec. 1.4 and Sec. 1.5 in order to evaluate the normal contact forces. In the next sections, the time-discrete vectors notations are lightened such as $\{\bullet(t_i)\}_{i=1\ldots N_\mathrm{t}} = \bullet$.

1.4 Dynamic Lagrangian Frequency Time Harmonic Balance

The Dynamic Lagrangian Frequency Time associated with the HBM (DLFT-HBM)[20] is widely used to compute the nonlinear response of blade/disk assemblies due to the dry friction at the root of the blades [22, 23]. This methodology relies on augmented lagrangians and uses a prediction-correction procedure in the time domain in

order to satisfy unilateral contact conditions. The augmented lagrangians strategy consists in writing the contact forces as follows,

$$\widetilde{\mathbf{f}}^{\mathrm{N}}_{\mathrm{nl,r}} = -\mathbf{Z}_{\mathrm{r}}\widetilde{\mathbf{x}}_{\mathrm{r}} - \varepsilon(\widetilde{\mathbf{g}}_{\mathbf{x},\mathrm{r}} - \widetilde{\mathbf{g}}_{\mathbf{y},\mathrm{r}}) \tag{14}$$

where $\widetilde{\mathbf{g}}_{\mathbf{x},\mathrm{r}} = \widetilde{\mathbf{x}}_{\mathrm{r}} - \mathbf{Fd}$ and $\widetilde{\mathbf{g}}_{\mathbf{y},\mathrm{r}} = \widetilde{\mathbf{y}}_{\mathrm{r}} - \mathbf{Fd}$ are the gap functions in the frequency domain, $\mathbf{d}$ is the time-discrete function that contains the distance $d(t)$ between the undeformed structure and the obstacle at each instant of the time discretization, ε is a numerical weighting factor and $\widetilde{\mathbf{x}}_{\mathrm{r}}$ the estimation of the solution provided by the Newton-Raphson algorithm at one iteration. One may note that even if it is often referred to as a *penalty parameter*, it is not equivalent to a penalty stiffness. The strategy relies on the introduction of a new unknown $\widetilde{\mathbf{y}}_{\mathrm{r}}$ that is implicitely calculated through the AFT procedure under the hypothesis that $\widetilde{\mathbf{y}}_{\mathrm{r}}$ is strictly admissible in terms of unilateral constraints. In order to compute $\widetilde{\mathbf{f}}^{\mathrm{N}}_{\mathrm{nl,r}}$, it is necessary to use a prediction-correction scheme, such as $\widetilde{\mathbf{f}}^{\mathrm{N}}_{\mathrm{nl,r}} = \widetilde{\mathbf{f}}^{\mathrm{N}}_{\mathrm{nl,pre}} + \widetilde{\mathbf{f}}^{\mathrm{N}}_{\mathrm{nl,cor}}$ where $\widetilde{\mathbf{f}}^{\mathrm{N}}_{\mathrm{nl,pre}} = -\mathbf{Z}_{\mathrm{r}}\widetilde{\mathbf{x}}_{\mathrm{r}} - \varepsilon\widetilde{\mathbf{g}}_{\mathbf{x},\mathrm{r}}$ and $\widetilde{\mathbf{f}}^{\mathrm{N}}_{\mathrm{nl,cor}} = \varepsilon\widetilde{\mathbf{g}}_{\mathbf{y},\mathrm{r}}$. The calculation of the correction term is conducted in the time domain, it is then necessary to use an IDFT on $\widetilde{\mathbf{f}}^{\mathrm{N}}_{\mathrm{nl,pre}}$ and apply the unilateral contact contraints at each time instant t_i of the discretized period:

- if $\mathbf{f}^{\mathrm{N}}_{\mathrm{nl,pre}}(t_i) > 0$, contact is detected then $\mathbf{g}_{\mathbf{y},\mathrm{r}}(t_i) = 0$ implying that $\mathbf{f}^{\mathrm{N}}_{\mathrm{nl,cor}}(t_i) = 0$,
- if $\mathbf{f}^{\mathrm{N}}_{\mathrm{nl,pre}}(t_i) \leq 0$, contact is not detected then $\mathbf{g}_{\mathbf{y},\mathrm{r}}(t_i) \neq 0$ implying that $\mathbf{f}^{\mathrm{N}}_{\mathrm{nl,r}}(t_i) = 0$ thus the correction should be $\mathbf{f}^{\mathrm{N}}_{\mathrm{nl,cor}}(t_i) = -\mathbf{f}^{\mathrm{N}}_{\mathrm{nl,pre}}(t_i)$.

The correction implies that the contact forces $\mathbf{f}^{\mathrm{N}}_{\mathrm{nl,r}}(t)$ and the gap function $\mathbf{g}_{\mathbf{y},\mathrm{r}}(t)$ strictly respect the Hertz-Signorini-Moreau conditions in the time domain:

$$\mathbf{0} \leq \mathbf{f}^{\mathrm{N}}_{\mathrm{nl,r}} \perp \mathbf{g}_{\mathbf{y},\mathrm{r}} \geq \mathbf{0} \tag{15}$$

A DFT is then applied on $\mathbf{f}^{\mathrm{N}}_{\mathrm{nl,r}}(t)$ in order to compute the residual function $\mathbf{H}_{\mathrm{r}}(\widetilde{\mathbf{x}}_{\mathrm{r}}, \omega)$:

$$\mathbf{H}_{\mathrm{r}}(\widetilde{\mathbf{x}}_{\mathrm{r}}, \omega) = \mathbf{Z}_{\mathrm{r}}(\omega)\widetilde{\mathbf{x}}_{\mathrm{r}} \underbrace{-\mathbf{Z}_{\mathrm{r}}\widetilde{\mathbf{x}}_{\mathrm{r}} - \varepsilon(\widetilde{\mathbf{g}}_{\mathbf{x},\mathrm{r}} - \widetilde{\mathbf{g}}_{\mathbf{y},\mathrm{r}})}_{\widetilde{\mathbf{f}}_{\mathrm{nl,r}}} \tag{16}$$

$$= -\varepsilon(\widetilde{\mathbf{g}}_{\mathbf{x},\mathrm{r}} - \widetilde{\mathbf{g}}_{\mathbf{y},\mathrm{r}}) \tag{17}$$

The expression of the DLFT-HBM residual (17) underlines that once the displacement field $\widetilde{\mathbf{x}}_{\mathrm{r}}$ satifies $\mathbf{H}_{\mathrm{r}}(\widetilde{\mathbf{x}}_{\mathrm{r}}, \omega) = \mathbf{0}^*$, the enforcement of the unilateral contact constraints is ensured by (17). The equation of motion is also satisfied, since if $\widetilde{\mathbf{g}}_{\mathbf{x},\mathrm{r}} - \widetilde{\mathbf{g}}_{\mathbf{y},\mathrm{r}} = \mathbf{0}$ is true, as (14) stands for the equation of motion by construction. The unilateral conditions (—) approximated by the DLFT-HBM are represented in Fig. 1. In this article, the weighting parameter ε is set at $1 \cdot 10^7\,\mathrm{N{\cdot}m^{-1}}$.

1.5 Regularized-Lanczos Harmonic Balance

The RL-HBM, which is the association of a regularized penalty law with the Lanczos filtering in a HB framework, was recently introduced [14].

In order to lift the indeterminacy of the contact forces with respect to the gap function, an explicit expression for the contact forces is used. Among existing contact laws, the penalty law reads:

$$f^{\mathrm{N}}_{\mathrm{nl}}(t) = -\kappa \max(0, g(t)) \tag{18}$$

Where κ is the penalty stiffness and $g(t) = x(t) - d(t)$ the gap function. This law allows some residual penetration between the structures since the gap function has to become negative for contact forces to appear. The penalty stiffness must be chosen as high as possible in order to approach the unilateral law, however in general κ can not take too high values since it also degrades the numerical stability of the algorithm. Thus, its value is related to a compromise between numerical stability and model accuracy. This bilinear contact law is actually still too severe numerically to be used in an AFT procedure, mainly because of its non-differentiability around $g(t) = 0$. For that

reason, the RL-HBM relies on a regularized approximation of this law (—), see Fig. 1. In order to smoothen the non-differentiability, a regularization parameter γ [14] is introduced in (18):

$$f_{\mathrm{nl}}^{\mathrm{N}}(t) = -\kappa \frac{g(t)}{2} + \sqrt{\left(\kappa \frac{g(t)}{2}\right)^2 + \gamma^2} \tag{19}$$

Thanks to the introduction of γ, the non-differentiability vanishes. While it may be convenient from a numerical standpoint, this formulation implies that contact forces are always nonzero, even for a positive gap. It underlines that γ should not be too high in order not to deteriorate the quality of the contact treatment. It is possible to note that the classical penalty law (18) is the particular case $\gamma = 0$ of the regularized law (19). In this paper, the penalty stiffness κ is $1 \cdot 10^9\,\mathrm{N{\cdot}m^{-1}}$ and the regularization parameter γ is $600\,\mathrm{N}$.

In addition to the regularization of the contact law, the RL-HBM features a filtering of the normal contact forces conducted by means of a Lanczos filter. This filtering is done during the transformation back to the frequency domain thanks to the introduction of the σ_k coefficients in the Fourier decomposition,

$$\mathbf{f}_{\mathrm{nl}}(\mathbf{x}, \dot{\mathbf{x}}) \simeq \frac{1}{2}\mathbf{a}_0^{\mathrm{nl}} + \sum_{k=1}^{N_{\mathrm{h}}} \sigma_k \left(\mathbf{a}_k^{\mathrm{nl}} \cos(k\omega t) + \mathbf{b}_k^{\mathrm{nl}} \sin(k\omega t)\right) \tag{20}$$

where:

$$\sigma_k = \mathrm{sinc}(\chi_k) \;\text{ where }\; \chi_k = \begin{cases} 0 & \text{for } k < 1 \\ \dfrac{k}{N_{\mathrm{h}}+1} & \text{for } 1 \leq k \leq N_{\mathrm{h}} \end{cases} \tag{21}$$

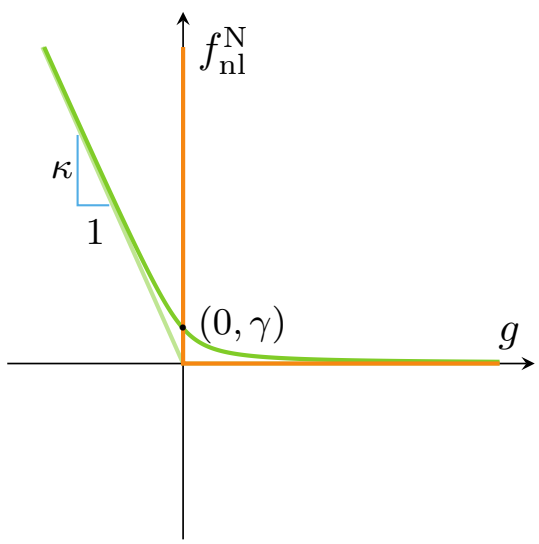

Figure 1. Contact laws: penalty law (—), regularized penalty law (—), unilateral law (—).

1.6 Path following

The nonlinear forces in the equation of motion usually induce sophisticated vibration responses. It was shown that, in the case of contact interactions, turning points appear [14, 24]. These limit points imply that the nonlinear equations admit coexisting solutions at a given pulsation ω. In order not to miss portions of the nonlinear frequency response curves (NFRC), one must employ a so called path continuation technique [24, 25] allowing to capture a

greater number of solutions than a regular frequency sweep. Continuation techniques are built upon the hypothesis of local continuity of the solution branches with respect to the control parameter, the pulsation ω in the present case. Among the multiple path continuation techniques that may be found in the literature, arc-length continuation may be the most commonly used in the field of nonlinear dynamics, this technique is considered in this paper. This prediction/correction methodology is defined by three key elements: the local parameterization of the curve, the prediction step and the correction steps.

Parameterization

The arc-length continuation relies on a local parameterization of the curve based on the arc-length parameter s, usually referred to as the curvilinear abscissa. The control parameter ω is considered as a new unknown of the problem, requiring the addition of (22) in order to close the system of equations:

$$\mathcal{P}(\widetilde{\mathbf{x}}_i^k, \omega_i^k) = \left\|\widetilde{\mathbf{x}}_i^k - \widetilde{\mathbf{x}}_{i-1}\right\|^2 + (\omega_i^k - \omega_{i-1})^2 - \Delta s_{i-1}^2 \tag{22}$$

The solutions are then found at the intersection of the space of solutions and the hypersphere of radius Δs_{i-1} centered around the previous solution point $\mathbf{y}_{i-1} = (\widetilde{\mathbf{x}}_{i-1}, \omega_{i-1})^\top$. The parameterization strategy (—) is displayed in Fig. 2a.

Prediction

In order to provide a good estimate of the solution to the nonlinear solver, a secant prediction is obtained using the last two points of the NFRC $\mathbf{y}_i$ and $\mathbf{y}_{i-1}$:

$$\mathbf{y}_{i+1}^0 = \mathbf{y}_i + \Delta s_i \frac{\Delta \mathbf{y}_i}{\|\Delta \mathbf{y}_i\|_2}, \text{ with } \Delta \mathbf{y}_i = \mathbf{y}_i - \mathbf{y}_{i-1} \tag{23}$$

This prediction is a relatively good estimate of the solution at no expense if Δs_i is sufficiently small, which is generally the case. The distance Δs_i should be the same as the one appearing in the parameterization (22) such that the prediction (23) is already on the hypersphere of research. This prediction (○) is illustrated in Fig. 2a.

Correction

Once a prediction has been made, it is necessary to correct the guess $\mathbf{y}_{i+1}^0$ to the actual solution. A Newton-Raphson algorithm is employed on the augmented system, including ω as a new unknown. The resulting nonlinear system reads,

$$\begin{pmatrix} \mathbf{H}(\mathbf{y}) \\ \mathcal{P}(\mathbf{y}) \end{pmatrix} = \mathbf{0} \tag{24}$$

This system is solved iteratively as follows,

$$\begin{pmatrix} \dfrac{\partial \mathbf{H}}{\partial \widetilde{\mathbf{x}}}(\mathbf{y}^k) & \dfrac{\partial \mathbf{H}}{\partial \omega}(\mathbf{y}^k) \\ \dfrac{\partial \mathcal{P}}{\partial \widetilde{\mathbf{x}}}(\mathbf{y}^k) & \dfrac{\partial \mathcal{P}}{\partial \omega}(\mathbf{y}^k) \end{pmatrix} \Delta \mathbf{y}^{k+1} = - \begin{pmatrix} \mathbf{H}(\mathbf{y}^k) \\ \mathcal{P}(\mathbf{y}^k) \end{pmatrix} \tag{25}$$

With $\mathbf{y}^{k+1} = \mathbf{y}^k + \Delta \mathbf{y}^{k+1}$ being the next iterate of the algorithm. The same criteria as given in Sec. 1.1 is used in order to assess the convergence of the solution. An illustration of the iterates (○) is displayed in Fig. 2a.

Closed loop control

When dealing with highly nonlinear phenomena, isolated solution branches can appear. In order to ensure that the continuation procedure does not loop over an isolated branch, it is a good practice to implement a closed loop detection throughout the calculation of the NFRC. A simple geometric condition is used in this paper. At the start of the continuation procedure, the point $\mathbf{y}_0 = (\widetilde{\mathbf{x}}_0, \omega_0)$ is chosen as a reference point, then if two successive points are

calculated such as $\omega_i < \omega_0 < \omega_{i+1}$ (or the other way around), a closed loop test is conducted. In order to carry out this test, it is necessary to interpolate between $\widetilde{\mathbf{x}}_i$ and $\widetilde{\mathbf{x}}_{i+1}$ at the pulsation ω_0, such as this interpolation $\widetilde{\mathbf{x}}_{\text{int}}$ reads:

$$\widetilde{\mathbf{x}}_{\text{int}} = \widetilde{\mathbf{x}}_i + \frac{\omega_0 - \omega_i}{\omega_{i+1} - \omega_i}(\widetilde{\mathbf{x}}_{i+1} - \widetilde{\mathbf{x}}_i) \tag{26}$$

The relative distance d_{int} between the interpolated point $\widetilde{\mathbf{x}}_{\text{int}}$ and the reference point $\widetilde{\mathbf{x}}_0$ is calculated such as,

$$d_{\text{int}} = \frac{\|\widetilde{\mathbf{x}}_{\text{int}} - \widetilde{\mathbf{x}}_0\|_2}{\|\widetilde{\mathbf{x}}_{\text{int}}\|_2} \tag{27}$$

If this distance is smaller than the value $d_{\min}$ given by the user, then the continuation stops as the NFRC has gone through the first point $\mathbf{y}_0$ again, thus forming a closed loop. This procedure is shown in Fig. 2b. An alternate method consists in correcting the interpolated $\widetilde{\mathbf{x}}_{\text{int}}$ point onto the NFRC thanks to a Newton-Raphson algorithm, but it induces an additional computational cost and the success of the method depends on the basin of attraction of the nonlinear function. For these reasons, the latter is not considered in this article.

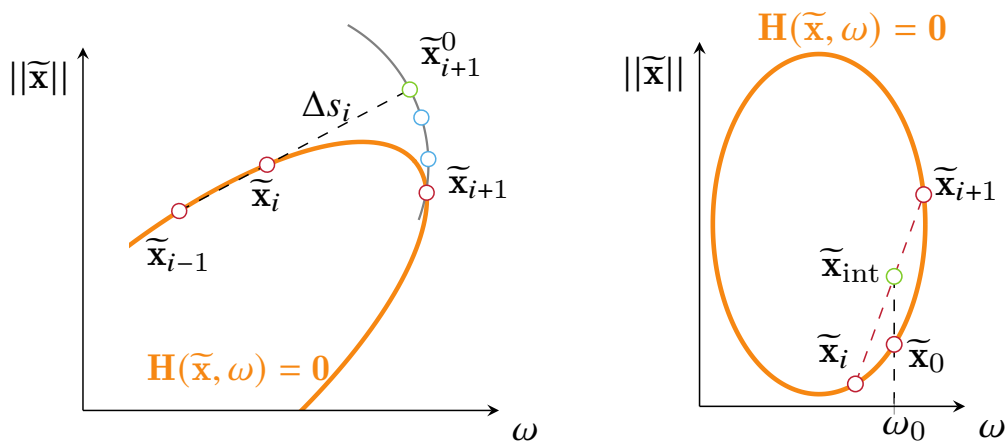

(a) parameterization and prediction

(b) isolas detection strategy

Figure 2. Continuation strategy, solutions subspace (—), direction of research (—), solutions (○), prediction (○), correction iterations (○).

2 BLADE TIP/CASING INTERACTION ON NASA ROTOR 67

2.1 Blade model

The industrial case study used to analyze the methodologies is the NASA rotor 67 [26]. It was initially designed at the NASA Lewis research center (Cleveland, Ohio, USA) as a reference geometry for research in fluid dynamics [27]. This geometry was recently used in a structural mechanics study [28] where its sophisticated dynamical response was exhibited. The material properties of this blade are not explicitly given in the initial report, however several articles make the assumption that this rotor is made out of the classical alloy composing fan blades: a titanium alloy TA6V of grade 5 (Ti 6Al 4V). The material properties retained for this study are given in Tab. 1

The full finite element mesh of the blade is composed of 129181 quadratic pentahedron elements for a total of 201287 nodes[1], see Fig. 3b. The nodes belonging to the root of the blade (—) are clamped. A reduced-order

[1]mesh available at `https://lava-wiki.meca.polymtl.ca/public/modeles/rotor_67/`

Young modulus E	Density ρ	Poisson coefficient ν
108 GPa	4400 kg·m^{-3}	0.34

Table 1. Material properties retained for TA6V.

model is computed with the Craig-Bampton method [29]. The reduced-order model is composed of $n_\mathrm{b} = 9$ boundary nodes (●) retained for contact management purposes and $\eta = 12$ modal dof. The size of the reduced-order model is $n = 3n_\mathrm{b} + \eta = 39$ dof with a total of 27 nonlinear dof. The structural damping is $\xi_{1-3} = 1 \cdot 10^{-3}$ for the first three modes (first bending mode (1B), second bending mode (2B) and first torsional mode (1T)) and $\xi_{4+} = 5 \cdot 10^{-3}$ for all the other modes. The eigenfrequencies for the modes of interest are given in Tab. 2. The full bladed disk is represented in Fig. 3a. For this study, a single blade is considered.

mode	1B	2B	1T
ω(rad·s^{-1})	2039.6	6339.7	10735.1
f(Hz)	324.6	1009	1708.5

Table 2. First eigenfrequencies of the blade.

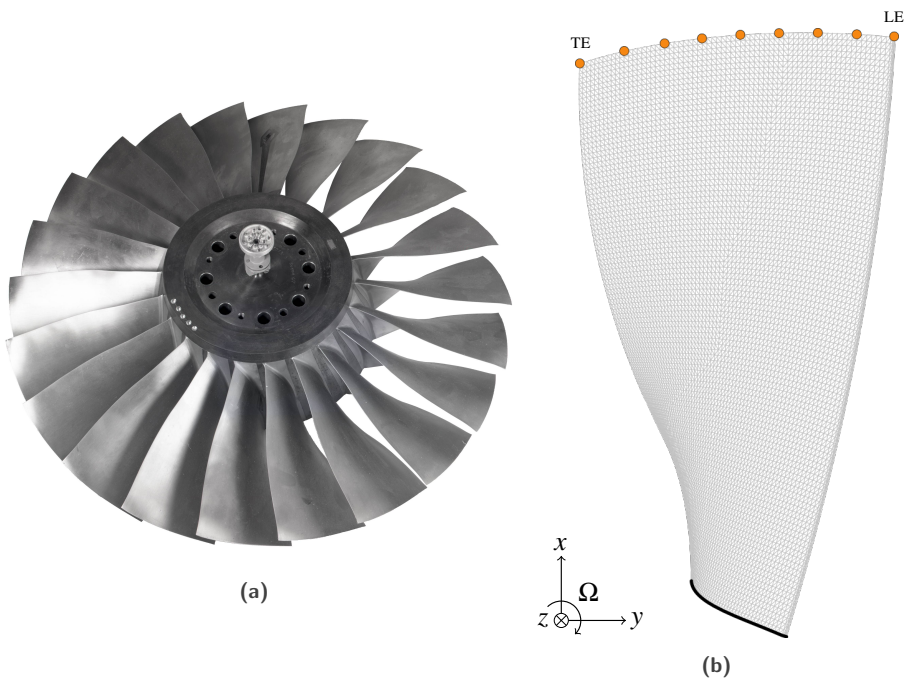

Figure 3. NASA rotor 67: full bladed disk [30] (a), finite element mesh (b).

2.2 Contact scenario

Rubbing interactions were experimentally observed under vacuum [31], for that reason, no aerodynamic forcing is considered. In fact, contact initiation is usually attributed to both centrifugal loads on the blades lowering the radial gap at the tip and thermal effects distorting the casing. Moreover, experimental observations underlined that the vibration amplitudes of the casing can be considered as negligible, justifying that the casing can be modeled as

a rigid profile. Considering the arguments presented, the casing is represented by a distorted and perfectly rigid mathematical profile. In agreement with previously published investigations on blade-tip/casing interactions [14, 16], the casing is ovalized thus privileging two symmetrical contact areas along the circumference of the casing for contact interactions. Due to the distortion of the casing, rubbing interactions occur at any angular speed. Moreover, the absence of external forcing allows to highlight contact-induced multiharmonic, multimodal and highly nonlinear responses. To the contrary, an harmonic external forcing usually favors responses on the pulsation of excitation around a specific mode of the structure, thus simplifying the type of dynamical response. The range of angular speeds Ω investigated in this paper is $\Omega \in [400, 2000]\,\mathrm{rad{\cdot}s^{-1}}$. In the frequency domain framework, the angular pulsation of resolution is the angular pulsation associated to the rotation of the blade such as $\omega = \Omega$.

2.3 Casing distortion

In order to take the casing distortion into account in the harmonic simulations, the latter is represented as a T-periodic distance function. This distance function is different for each boundary node $j \in [\![1, n_\mathrm{b}]\!]$ and it reads:

$$d_j(\tau) = c_j - (c_j + p_j)\exp\left[-\left(\frac{(\tau+\theta_j)(2\pi \bmod n_\mathrm{l}) - \dfrac{\pi}{n_\mathrm{l}}}{w_\mathrm{l}}\right)^2\right] \tag{28}$$

where τ is the normalized time related to the angular speed of the blade, θ_j is the angular shift of the boundary node due to the twist of the blade measured on the mesh, c_j is the operating clearance, p_j is the penetration of the lobes with the blade's circular trajectory corresponding to its linear behaviour, w_l is a weight standing for the angular width of the lobes and n_l is the number of lobes. For this study, the following values are used: $n_\mathrm{l} = 2$, $w_\mathrm{l} = 0.15$ and for all boundary nodes $c_j = 4 \cdot 10^{-4}\,\mathrm{m}$ and $p_j = 1.25 \cdot 10^{-4}\,\mathrm{m}$. The shape of the casing is similar for all contact nodes, it is only angularly offset with different values of θ_j to compensate the twist of the blade, since the lobe is aligned with the axial direction. The shape of one lobe is shown in Fig. 4.

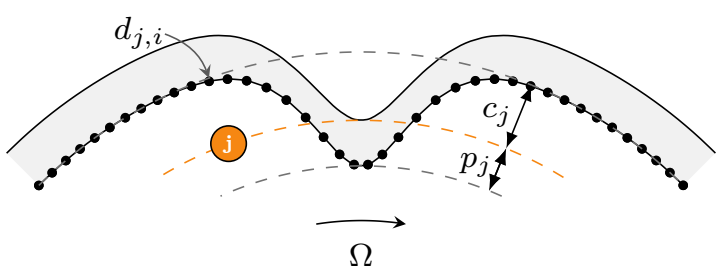

Figure 4. One lobe distortion of the casing (▭) in front of the j-TH boundary node (●).

2.4 Friction management

Normal contact is assumed to be solely along the radial direction, which makes the radial displacement of the boundary nodes $r_j(t)$ with $j \in [\![1, n_\mathrm{b}]\!]$ the quantities of interest. Moreover, for both DLFT-HBM and RL-HBM, whenever a radial contact is detected, say at time t_i, it is necessary to compute the dry friction forces in the tangential directions (θ, z). Given the very high relative speeds between the blade tip and the casing, permanent sliding is assumed thus simplifying the computation of friction forces. Both circumferential f^θ_nl and axial f^z_nl forces can be expressed according to the Coulomb's Law in sliding such as,

$$f^\theta_{\mathrm{nl},j}(t_i) = \mu \frac{v_\theta(t_i) + \rho_j\Omega}{\sqrt{(v_\theta(t_i) + \rho_j\Omega)^2 + v_z(t_i)^2}} f^\mathrm{N}_\mathrm{nl}(t_i) \tag{29}$$

$$f^{z}_{\mathrm{nl},j}(t_i) = \mu \frac{v_z(t_i)}{\sqrt{(v_\theta(t_i) + \rho_j \Omega)^2 + v_z(t_i)^2}} f^{\mathrm{N}}_{\mathrm{nl}}(t_i) \tag{30}$$

where the friction coefficient μ is 0.15, v_θ is the circumferential vibration velocity, v_z the axial vibration velocity, and ρ_j the radial position of the j-th boundary node with respect to the axis of rotation.

3 NUMERICAL RESULTS

In order to confront the different solution methods on the presented problem, a time integration (TI) analysis is carried out in Sec. 3.1, then the analysis of the HB strategies' results is conducted in Sec. 3.2, in the end a thorough analysis is done on the isolated frequency response curves in Sec. 3.4.

3.1 Time-domain reference results

The reference time integration strategy is a state-of-the-art methodology used in the turbomachinery industry to evaluate the criticity of rubbing interactions [3, 15]. It is used in this paper for a frequency sweep on the angular speed range in order to provide the nonlinear frequency response curve in the light of the time domain paradigm. This frequency sweep is represented in Fig. 5. Each point represents a simulation over 200 revolutions starting from null initial conditions with a time step $\mathrm{d}t = 1 \cdot 10^{-7}$ s. The order of magnitude associated with the calculation of each point is around two minutes of CPU time on a 8 cores i7 CPU.

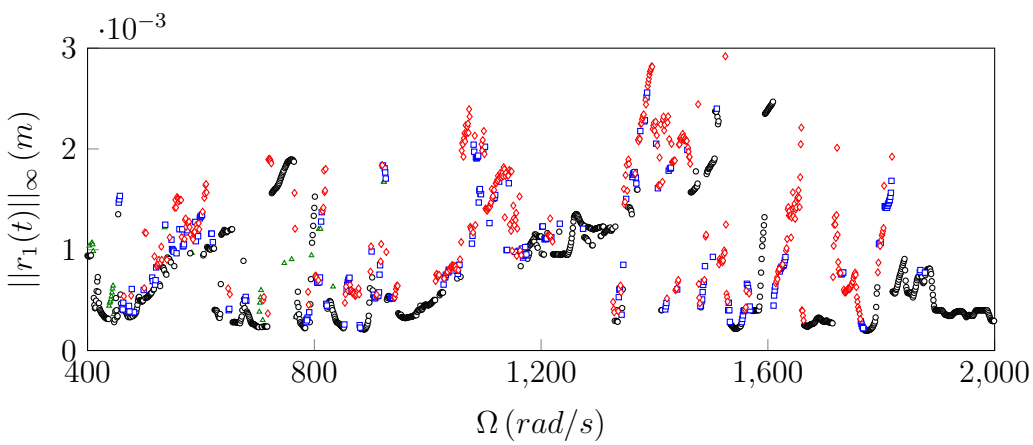

Figure 5. NFRC obtained through TI at the LE, fundamental pulsation ω: $\omega = 2\Omega$ (●), $\omega = \Omega$ (▲), subharmonic ($\omega < \Omega$) (■), no periodicity or $\omega < \Omega/10$ (♦).

From the perspective given by the time-marching results, the dynamical response of the system seems to be complex, and no trend can be easily identified in terms of amplitude. A periodicity analysis is conducted on the time signals in order to have a better understanding of the complex dynamics involved. Several behaviours are detected through TI. Firsly, periodic responses synchronized with the periodicity of the casing $\omega = 2\Omega$ (●) are obtained. Periodic solutions of fundamental pulsation $\omega = \Omega$ (▲) are also detected, these responses are technically period-doubled relative to the periodicity of the casing. The third type of responses are subharmonic with respect to the angular speed Ω (■), that may have emerged through multiple period-doubling bifurcations. Also, solutions featuring no periodicity are found (♦) i.e. quasi-periodic, aperiodic or even chaotic responses. The fact that the blade's response features a variable periodicity lays out a very challenging context for the use of frequency domain methodologies. In this paper, the fundamental frequency of resolution for the HB strategies is chosen to be $\omega = \Omega$, thus categories (■) and (♦) cannot be captured. Though, should subharmonic responses (■) be of interest, it would be possible to lower the resolution frequency such as $\omega = \Omega/\nu$ with $\nu > 1$ in order to capture them. In the rest of

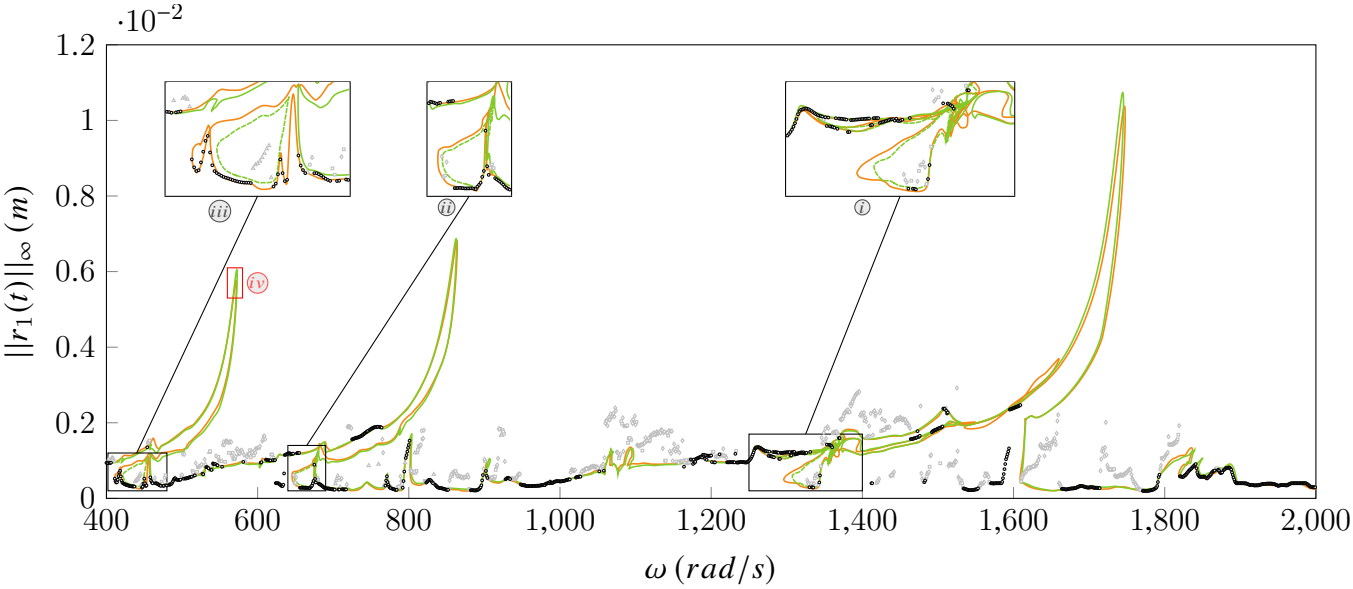

Figure 6. NFRC obtained through HB methods, DLFT-HBM (—), RL-HBM (—), RL-HBM isolas (-----), IT of fundamental pulsation ω: $\omega = 2\Omega$ (●), $\omega = \Omega$ (▲), subharmonic ($\omega < \Omega$) (■), no periodicity or $\omega < \Omega/10$ (♦).

the article, since the emphasis is put on 2Ω-periodic solutions (●), all other three categories are colored in gray for the sake of readability : (♦),(▲),(■).

3.2 Harmonic analysis of the interactions

In this section, both HB strategies are used to obtain NFRC for the considered rubbing interactions. Both methodologies use the same number of harmonics $N_\mathrm{h} = 40$ and number of time instants $N_\mathrm{t} = 1024$. The results are displayed in the form of amplitude curves at the leading edge in the radial direction in Fig. 6 and are obtained by a path continuation procedure. The time domain NFRC is also superimposed in order to provide reference results. The order of magnitude associated with both HBM computations of the NFRC is between 30 and 60 minutes of CPU time on a 8 cores i7 CPU. Computation times are similar for both methods. Firstly, the DLFT-HBM (—) and RL-HBM (—) show a very good agreement between each other over the whole NFRC. Three areas of discrepancy are identified and are shown in the i , ii and iii frames. In these frames, the DLFT-HBM captures portions of the NFRC that RL-HBM does not. In order to investigate these differences and to verify that the DLFT-HBM solutions are valid, the RL-HBM was initialized with DLFT-HBM solutions on these specific frequency ranges. The obtained curves (-----) are displayed in Fig. 6. The identified areas of discrepancy are in fact isolated frequency response curves for the RL-HBM. This phenomenon is more clearly observed on frame iii where it may be seen that the curve is forming a closed loop. This shows that the results are highly sensitive to contact laws. Indeed, both methodologies give similar results on the whole frequency range, even though both strategies use different contact laws. However, these differences of contact treatment have the impact of disconnecting solution branches from the primary NFRC in the case of RL-HBM. These disconnections are not easily attributed to one aspect or another of the methodologies and would require a dedicated study. Indeed, no convergence or parametric study was led beforehand on the contact law parameters (ε for DLFT-HBM and (κ, γ) for RL-HBM) or even on the influence of filtering. The excellent correlation of the strategies with each other as well as with the time paradigm results—without any prior convergence analysis—underlines their robustness. On another aspect, the areas of discrepancy also highlight the sensitivity of the numerical solvers to the contact treatment related parameters. This sensitivity must be addressed in future work and is not critical since an excellent agreement is achieved everywhere but on these few areas.

Even if these disconnections seem to cause significant deviations from one method to the other, it must be

reminded that the branch continuity is one of the new qualitative aspects provided by harmonic strategies. Indeed, this type of conclusions would not be available with the sole use of time-domain methodologies. Indeed, time-marching algorithms are usually restrained to a single pulsation of resolution with no influence of previous points as no continuation is employed.

In order to assess the performance of the methodologies close to the nonlinear resonances, a zoomed and rescaled vision of the (iv) frame is represented in Fig. 7. This view underlines the presence of the spurious oscillations around the peak (also known as aliasing phenomenon [32]) for DLFT-HBM, whereas the filtering used in RL-HBM mitigates this numerical problem associated to the time discretization inside the AFT procedure. This phenomenon is usually responsible of a slowdown of the continuation procedure around nonlinear resonances and should be mitigated by increasing the time discretization which increases the overall computational cost.

When it comes to the paradigm confrontation, it is clear that the HB and TI strategies do not reflect the same high amplitude dynamics around the nonlinear resonances. Indeed, around these peaks, the amplitudes differ of a factor 5, which underlines the difficulties encountered by the time marching strategy to capture high amplitude solutions starting from null initial conditions. It is observed that the null initial conditions used by TI usually favors the convergence towards solutions with relatively low amplitudes. However, on the points where a periodic solution of fundamental pulsation $\omega = 2\Omega$ (•) the TI results are in agreement with the HB strategies.

On Fig. 6, two angular speed ranges where significant amplitude discrepancies are observed: $\Omega \in [1400, 1600]\text{rad}\cdot\text{s}^{-1}$ and $\Omega \in [620, 635]\ \text{rad}\cdot\text{s}^{-1}$. In order to investigate these differences, the periodic solutions of fundamental pulsation 2Ω are used as an initialization for both HB strategies. This leads to the discovery of two isolated solution branches referred as ① and ④ on Fig. 8, as already shown in [28] for the same contact scenario. The existence of such solution branches is obvious for both ① and ④ because multiple TI periodic solutions are captured in a certain neighbourhood. However, it is also possible to check for HB solutions on every periodic TI solution available, this procedure leads to the discovery of the branches numbered ② , ③ and ⑧ . In order to have a wider view on the isolated branches, a specific study is led with the HB strategies: several frequency sweeps are realized with initialization conditions of different amplitudes A in the range $A \in [10^{-3}, 10^{-2}]$, this range is defined using the amplitudes observed on the primary NFRC. It has been observed that solutions along isolated branches experience dynamical responses concentrated on high order modal shapes (2B, 1T or higher) on a specific angular speed harmonic number (engine order). Following these observations, the initial conditions of the HBM solver for the frequency sweeps are chosen such as:

$$\mathbf{x}^0(t) = A\Phi_j \cos(k\Omega t) \tag{31}$$

where A is the dimensionless amplitude, Φ_j is the j-th modal shape, k the harmonic number and Ω the angular speed. This type of initialization allows to capture intersections of engine orders with modes in the angular speed/frequency response plane (interaction maps). The use of such frequency sweeps allows to find solutions on the already discovered isolas (without the use of the TI) as well as the discovery of even more isolas ⑤ , ⑥ and ⑦ .

The entirety of the results are represented in Fig. 8, this new NFRC allows for a more extended view of the initial NFRC represented in Fig. 6 but with the addition of multiple isolated solution branches. It is worth noting that this view—most probably—does not contain every solution branches since no explicit exhaustive research of isolated and bifurcated branches is conducted in this study. This constitutes a major roadblock to be addressed in future work. Several developpements already exist on the subject [10, 33, 34] but the applications are limited to systems with few degrees of freedom.

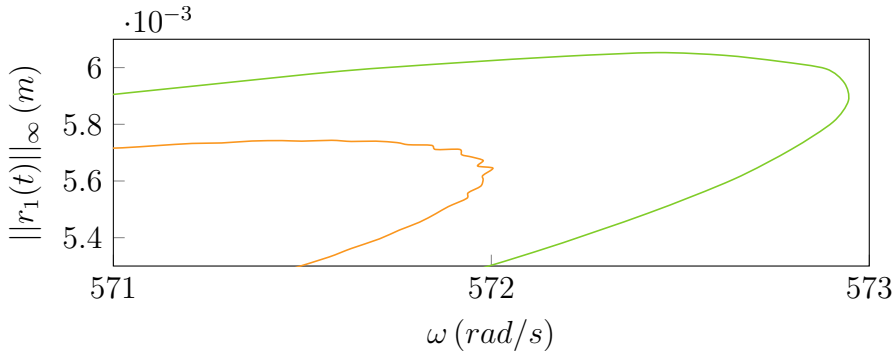

Figure 7. Rescaled view of the first resonance (frame *iv*) , DLFT-HBM (—), RL-HBM (—).

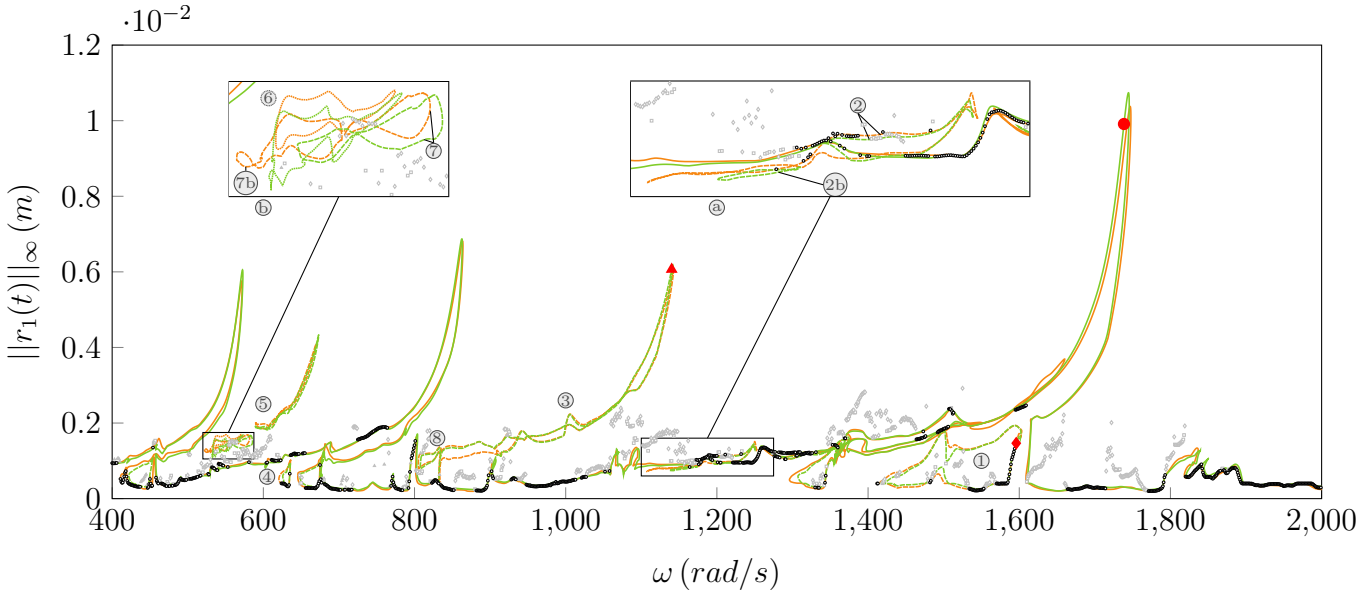

Figure 8. Full view of the blade's response obtained through HB methods with isolas, DLFT-HBM (—), RL-HBM (—), DLFT-HBM isolas (-----), RL-HBM isolas (-----), IT of fundamental pulsation ω: $\omega = 2\Omega$ (●), $\omega = \Omega$ (▲), subharmonic ($\omega < \Omega$) (■), no periodicity or $\omega < \Omega/10$ (♦).

Some of the periodic TI solutions of fundamental pulsation $\omega = \Omega$ (▲) allowed to find what can be qualified of period-doubled bifurcated branches. These branches are captured through both HB strategies but were not displayed in Fig. 8 for the sake of readability, except for the bifurcated branch number ③ that appears to be a high amplitude subharmonic resonance. This branch is subject to significant deviations from one method to the other: one of its two bifurcation points connecting it to the primary NFRC is not at the same location for both methodologies. However, this difference is not explored in this paper as the dynamics of the branch at resonance is not affected.

For almost all isolas, both methodologies are in accordance in terms of amplitude. However, two isolas demonstrate a specific behaviour: ② in ⓐ and ⑦ in ⓑ . Indeed, the isola ② forms a closed loop in DLFT-HBM, whereas it is divided in two separated isolas ② and 2b for RL-HBM. On the contrary, the opposite behaviour is observed for ⑦ where it forms a single loop for RL-HBM and two isolas ⑦ and 7b in DLFT-HBM. These facts were verified by providing one method with initializations on different portions of the isola obtained with the other method. This behaviour underlines once again the sensitivity of the results to the contact law: the contact model also influences

how the different solutions belonging to isolas are connected together.

Three points of interest are identified in Fig. 8: (●), (♦), (▲). These points are used to perform an in-depth comparative analysis on the time signals in Sec. 3.3

3.3 Time signals

The points displayed in Fig. 8 are located: near the nonlinear primary resonance (●), on isola ① (♦) and on the bifurcated branch ③ (▲). Corresponding time signals of radial displacement and contact forces are represented in Fig. 9, both at the leading edge (LE) and the trailing edge (TE). In order to compare the HB solutions to the time-marching strategy, the TI results are obtained by using the RL-HBM solutions to generate initial conditions, this choice is purely arbitrary and DLFT-HBM solutions could also be used. The solution is then time-marched for a hundred periods in order to ensure that a steady state has been reached. The results given in Fig. 9 underline

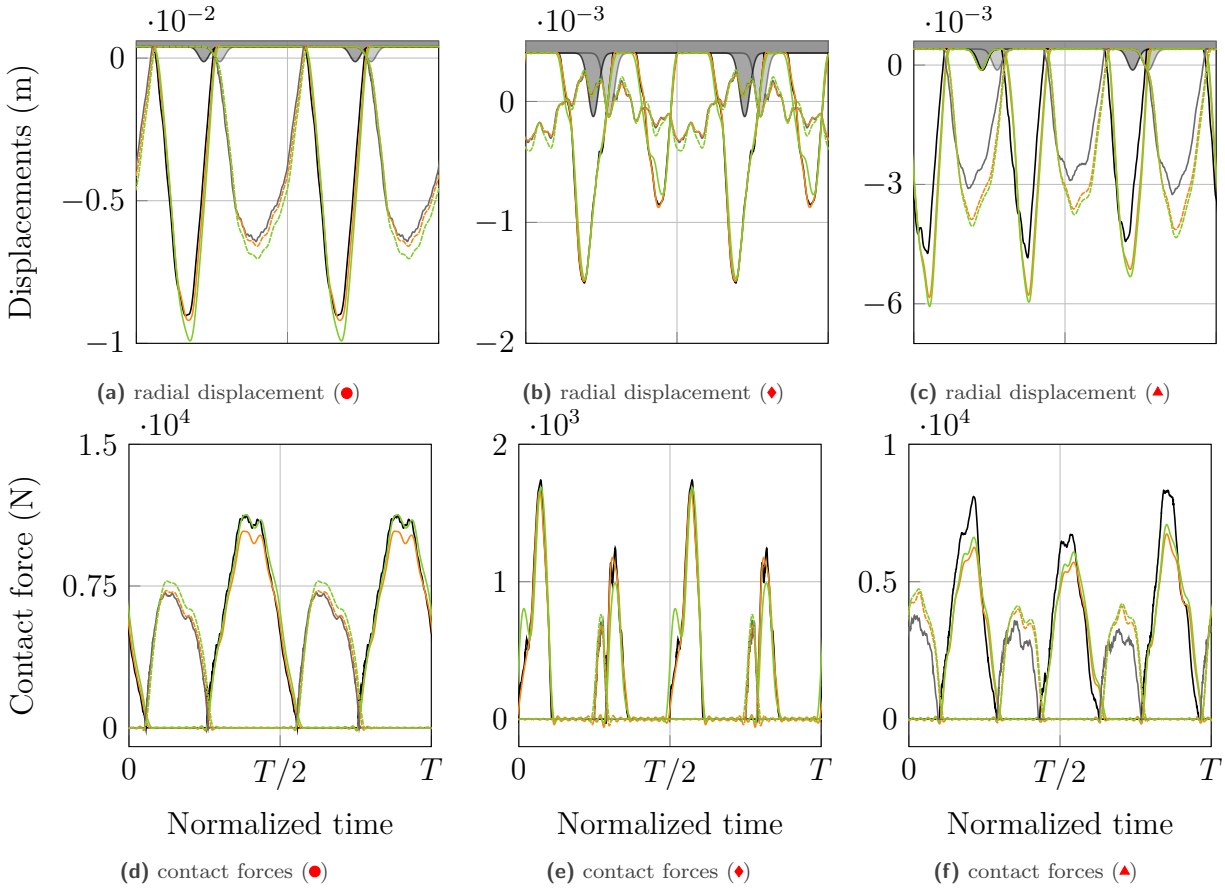

(a) radial displacement (●) **(b)** radial displacement (♦) **(c)** radial displacement (▲)

(d) contact forces (●) **(e)** contact forces (♦) **(f)** contact forces (▲)

Figure 9. Time signals of radial displacement and contact forces at the principal resonance (●), on the isola ① (♦) and branch ③ (▲) , DLFT-HBM: LE (—) TE (----), RL-HBM: LE (—) TE (----), TI: LE (—) TE (—).

the very good agreement of all three methodologies on the chosen points for both displacement and contact forces. At the nonlinear resonance and on isola ① , the DLFT-HBM seems to achieve a slightly higher accuracy on the amplitude of vibration whereas the RL-HBM is more accurate on the contact forces. Though, it is important to recall that —as a proof of robustness— no thorough parametric study was led on the contact treatment, thus this observation concerning accuracy must be mitigated and it may not be true if the contact treatment numerical parameters were different. In order to make a rigorous conclusion on this aspect, it would require a dedicated convergence analysis on both methodologies concerning the contact treatment parameters. It is possible to note

that the solutions on the branch ③ are of fundamental pulsation $\omega = \Omega$ unlike the other two points where the periodicity is that of the casing. In order to evaluate the differences generated by the contact law, it is necessary to investigate the behaviour of the strategies around the contact interface: the casing. A zoomed view around the casing is provided in Fig. 10 for the first boundary node (LE) and the second boundary node.

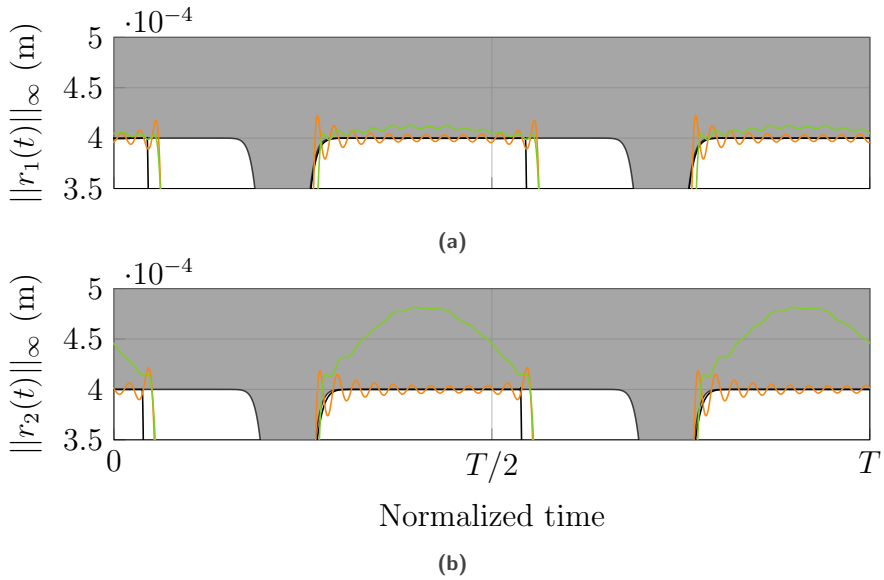

Figure 10. Time signals of radial displacement at the principal resonance (●) around the contact interface, DLFT-HBM (—), RL-HBM (—), TI (—), casing (▬).

The results represented in Fig. 10 highlight how RL-HBM and DLFT-HBM behave during a contact event. On the one hand, in Fig. 10a, the residual penetration is around the same order of magnitude for both contact laws. The influence of filtering on RL-HBM can be easily identified in comparison with DLFT-HBM. The latter experiences spurious oscillations that even have higher amplitude than the penetration generated through the penalty law of RL-HBM. This underlines that even if DLFT-HBM uses an augmented lagrangian formalism, it can experience larger residual penetrations than penalty laws in some situations. On the other hand, in Fig. 10b, the DLFT-HBM still experiences the oscillations with the same amplitude, however the residual penetration of RL-HBM is greatly increased. This phenomenon is related to higher values of the contact forces involved (not shown for the sake of brevity). This shows that both methodologies have specific behaviours during contact: (1) DLFT-HBM experiences large oscillations due to the Gibbs phenomenon but it is constant with the level of forces and (2) RL-HBM mitigates the oscillations with filtering but the residual penetration is a function of the level of the contact forces.

3.4 Dynamical content of isola 1

The isolas and bifurcated branches are usually associated with a specific dynamical content. This sophisticated content is explored in this section, on the application of rubbing interactions on isola ① .

In order to evaluate the dynamical content of the different HB solutions, modal coefficients are computed on each solution where the j-th modal contribution γ_j at time t_i reads:

$$\gamma_j(t_i) = \Phi_j^\top \mathbf{M}\mathbf{x}(t_i) \tag{32}$$

with Φ_j the j-th modal shape and $\mathbf{M}$ the mass matrix. For the needs of representation, the maximum modal relative contribution is considered:

$$||\gamma_j(t)||_{\infty,\text{rel}} = \frac{\max\limits_{i\in[\![1,N_\text{t}]\!]} |\gamma_j(t_i)|}{\sum\limits_{k=1}^{n} \max\limits_{i\in[\![1,N_\text{t}]\!]} |\gamma_k(t_i)|} \tag{33}$$

This formula is used to compute the relative modal contributions of the first four modes of the structure on isola ① . These coefficients are plotted in the z-direction of Fig. 11.

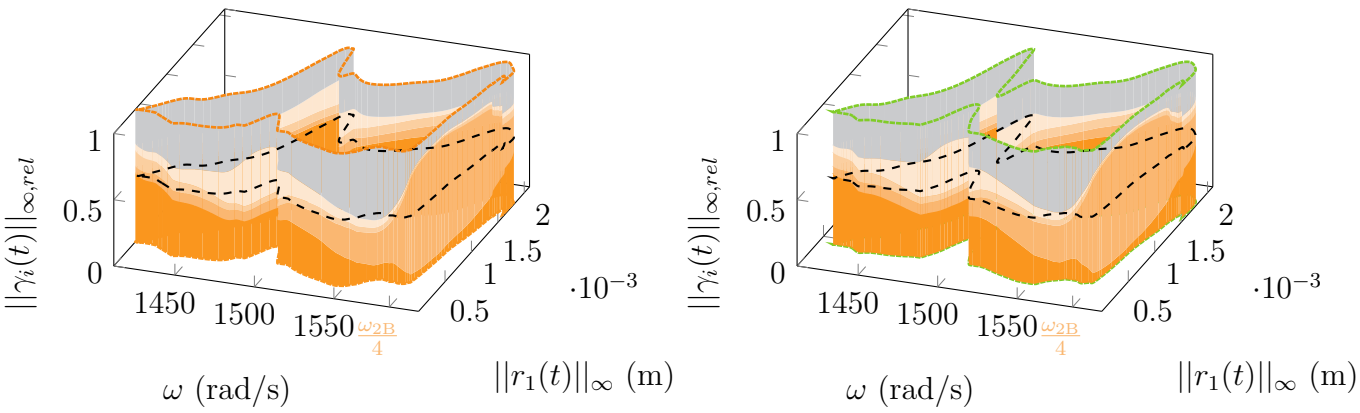

(a) DLFT-HBM **(b)** RL-HBM

Figure 11. Relative modal contributions on isola ① , 1B (■), 2B (■), 1T (□), 4th mode (□), all remaining modes (■), $||\gamma_i(t)||_{\infty,\text{rel}} = 0.5$ (- -).

In Fig. 11, a significant 2B contribution is detected around $\omega \simeq \omega_{2B}/4 = 1584.9\,\text{rad}\cdot\text{s}^{-1}$. A high participation of the 4th mode is also detected around $\omega \simeq \omega_4/10 = 1483\,\text{rad}\cdot\text{s}^{-1}$. In order to verify if these high participations are actually linked to the intersections of the different engine orders with the modes, the first ten harmonic contributions of the radial displacement at the LE $|c_{k,0}|$ are plotted in Fig. 12. The harmonic contributions of the j-th dof are calculated thanks to the Fourier coefficients:

$$|c_{k,j}| = \sqrt{a_{k,j}^2 + b_{k,j}^2} \tag{34}$$

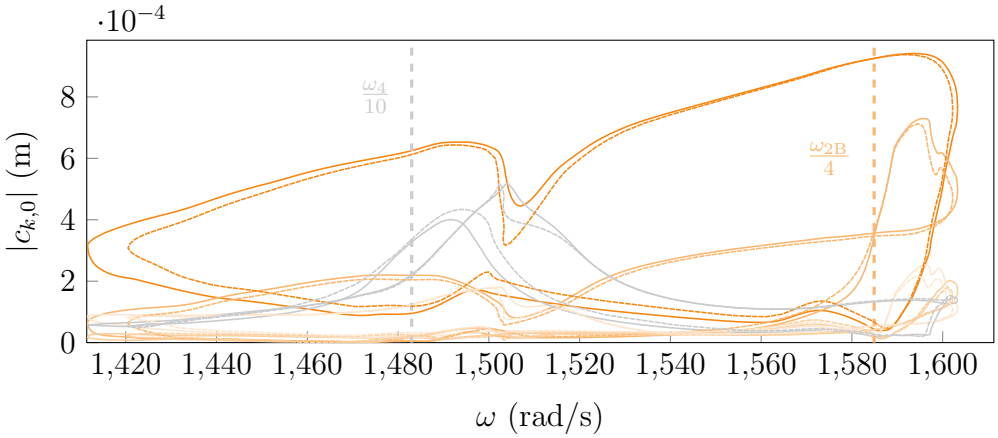

Figure 12. Harmonic contributions on isola ① , DLFT-HBM (—), RL-HBM (----), $k = 2$ (■), $k = 4$ (■), $k = 6$ (□), $k = 8$ (□), $k = 10$ (■).

It is clear that the intersections $\frac{\omega_{2B}}{4}$ (- -) and $\frac{\omega_4}{10}$ (- -) are linked to an increase of the contributions of respectively the 4th harmonic (—) and the 10th harmonic (—). This underlines how the isolas are generally associated with specific dynamical behaviours, whereas on the primary NFRC the blade mainly responds on the 1B mode and 2nd harmonic.

CONCLUSION

In this paper, two harmonic balance strategies are compared for the analysis of rubbing interactions in aeronautical turbomachines. Both methods are applied on the open geometry of the NASA rotor67. Due to the flexibility of this fan blade model, the highly nonlinear responses of the blade highlight some discrepancies between the strategies. The thorough comparative analysis on the nonlinear frequency response curves obtained through a continuation procedure shows an excellent agreement between both harmonic balance approaches around primary resonances. Though, some differences on limited frequency ranges are found in the form of isolas disconnecting from the primary response curve. Since the test case is identical for both HBM-based strategies, the associated deviation is necessarily linked to the use of different contact treatments and the addition of filtering for RL-HBM. This type of disconnection can also be observed when varying physical parameters such as the damping coefficient or the friction coefficient. However, these differences are of a new kind since the continuity of solutions along branches is not available when using the sole time marching approach. The use of the start-of-the-art time integration strategy allows to validate the precision of the frequency domain methodologies on multiple points. The excellent agreement of the three methodologies without prior contact treatment calibration underlines both the robustness and the industrial applicability of HBM-based strategies. A time-marching frequency sweep helped on the discovery of isolated nonlinear frequency response curves. One of these isolas is finely analyzed in terms of modal and harmonic contributions in order to conclude on its nature. Isolas are shown to experience dynamical responses along high order modes and high harmonics. Thanks to these new insights, it is possible to identify the intersections of engine orders with modes as areas of particular interest for the disconnection of isolated branches. Throughout this article, the complementarity of the time domain and frequency domain paradigms is highlighted since each method provides specific informations about the solutions to the rubbing interactions problem, and thus both must be used as completing tools. In this work, the DLFT-HBM strategy was applied to a new contact interface, the latter was already extensively used on friction-damping applications, however it was never used in the case blade-tip/casing interactions. Both HBM techniques may then be suitable to carry out original multi-nonlinear structural analyses accounting for various types of nonlinear interfaces.

Acknowledgments

This research was undertaken thanks to funding from the Canada Research Chairs Program.

References

[1] A. Batailly, M. Legrand, A. Millecamps, S. Cochon, and F. Garcin. Redesign of a High-Pressure Compressor Blade Accounting for Nonlinear Structural Interactions. J. Eng. Gas Turbines Power Vol. 137, No. 2 (2015), 022502. DOI: 10.1115/1.4028263. oai : hal-01120158.

[2] A. Batailly, M. Legrand, A. Millecamps, and F. Garcin. Numerical-Experimental Comparison in the Simulation of Rotor/Stator Interaction Through Blade-Tip/Abradable Coating Contact. J. Eng. Gas Turbines Power Vol. 134, No. 8 (2012), 082504. DOI: 10.1115/1.4006446. oai : hal-00746632.

[3] A. Millecamps, A. Batailly, M. Legrand, and F. Garcin. Snecma's Viewpoint on the Numerical and Experimental Simulation of Blade-Tip/Casing Unilateral Contacts. *Proceedings of the ASME Turbo Expo 2015: Turbine Technical Conference and Exposition*. Vol. 7B: Structures and Dynamics. Montreal, Quebec, Canada, 2015, V07BT32A014. DOI: 10.1115/GT2015-42682. oai : hal-01223582.

[4] K. E. Turner, C. Padova, and M. Dunn. Airfoil Deflection Characteristics During Rub Events. J. Turbomach. Vol. 134, No. 1 (2010), 11.

[5] M. Legrand and C. Pierre. Numerical Investigation of Abradable Coating Wear Through Plastic Constitutive Law: Application to Aircraft Engines. *Proceedings of the ASME 2009 International Design Engineering Technical Conferences and Computers and Information in Engineering Conference*. Vol. 1: 22nd Biennial Conference on Mechanical Vibration and Noise, Parts A and B. San Diego, California, USA, 2009, pp. 907–916. DOI: 10.1115/DETC2009-87669. oai : hal-00413728.

[6] R. J. Williams. Simulation of Blade Casing Interaction Phenomena in Gas Turbines Resulting From Heavy Tip Rubs Using an Implicit Time Marching Method. *Proceedings of the ASME 2011 Turbo Expo: Turbine Technical Conference and Exposition*. Vol. 6: Structures and Dynamics, Parts A and B. Vancouver, British Columbia, Canada, 2011, pp. 1007–1016. DOI: 10.1115/GT2011-45495. oai : hal-01555287.

[7] S. K. Sinha. Rotordynamic analysis of asymmetric turbofan rotor due to fan blade-loss event with contact-impact rub loads. J. Sound Vib. Vol. 332, No. 9 (2013), 2253–2283. DOI: 10.1016/j.jsv.2012.11.033. oai : hal-01555281.

[8] S. Nitschke, T. Wollmann, C. Ebert, T. Behnisch, A. Langkamp, T. Lang, E. Johann, and M. Gude. An advanced experimental method and test rig concept for investigating the dynamic blade-tip/casing interactions under engine-like mechanical conditions. Wear Vol. 422-423 (2019), 161–166. DOI: 10.1016/j.wear.2018.12.072.

[9] I. R. Praveen Krishna and C Padmanabhan. Experimental and numerical investigations on rotor–stator rub. Proceedings of the Institution of Mechanical Engineers, Part C: Journal of Mechanical Engineering Science Vol. 232, No. 18 (2018), 3200–3212. DOI: 10.1177/0954406217735348.

[10] L. Salles, B. Staples, N. Hoffmann, and C. Schwingshackl. Continuation techniques for analysis of whole aeroengine dynamics with imperfect bifurcations and isolated solutions. Nonlinear Dyn. Vol. 86, No. 3 (2016), 1897–1911. DOI: 10.1007/s11071-016-3003-y.

[11] P. Almeida, C. Gibert, F. Thouverez, X. Leblanc, and J.-P. Ousty. Numerical Analysis of Bladed Disk–Casing Contact With Friction and Wear. J. Eng. Gas Turbines Power Vol. 138, No. 12 (2016), 122802. DOI: 10.1115/1.4033065.

[12] N. Lesaffre, J.-J. Sinou, and F. Thouverez. Contact analysis of a flexible bladed-rotor. Eur. J. Mech. A. Solids Vol. 26, No. 3 (2007), 541–557. DOI: 10.1016/j.euromechsol.2006.11.002. oai : hal-00322887.

[13] E. P. Petrov. Multiharmonic Analysis of Nonlinear Whole Engine Dynamics With Bladed Disc-Casing Rubbing Contacts. *Proceedings of the ASME Turbo Expo 2012*. Vol. 7: Structures and Dynamics, Parts A and B. Copenhagen, Denmark, 2012, pp. 1181–1191. DOI: 10.1115/GT2012-68474.

[14] Y. Colaïtis and A. Batailly. The harmonic balance method with arc-length continuation in blade-tip/casing contact problems. J. Sound Vib. Vol. 502 (2021), 116070. DOI: 10.1016/j.jsv.2021.116070. oai : hal-03163560.

[15] N. J. Carpenter, R. L. Taylor, and M. G. Katona. Lagrange constraints for transient finite element surface contact. Int. J. Numer. Meth. Engng. Vol. 32, No. 1 (1991), 103–128. DOI: 10.1002/nme.1620320107. oai : hal-01389918.

[16] E. Piollet, F. Nyssen, and A. Batailly. Blade/casing rubbing interactions in aircraft engines: Numerical benchmark and design guidelines based on NASA rotor 37. J. Sound Vib. Vol. 460 (2019), 114878. DOI: 10.1016/j.jsv.2019.114878. oai : hal-02281666.

[17] E. P. Petrov. Analysis of Bifurcations in Multiharmonic Analysis of Nonlinear Forced Vibrations of Gas Turbine Engine Structures With Friction and Gaps. J. Eng. Gas Turbines Power Vol. 138, No. 10 (2015), 12.

[18] L. Peletan, S. Baguet, M. Torkhani, and G. Jacquet-Richardet. Quasi-periodic harmonic balance method for rubbing self-induced vibrations in rotor–stator dynamics. Nonlinear Dyn. Vol. 78, No. 4 (2014), 2501–2515. DOI: 10.1007/s11071-014-1606-8. oai : hal-01061265.

[19] H. Ma, X. Tai, Q. Han, Z. Wu, D. Wang, and B. Wen. A revised model for rubbing between rotating blade and elastic casing. J. Sound Vib. Vol. 337 (2015), 301–320. DOI: 10.1016/j.jsv.2014.10.020. oai : hal-01430515.

[20] S. Nacivet, C. Pierre, F. Thouverez, and L. Jezequel. A dynamic Lagrangian frequency–time method for the vibration of dry-friction-damped systems. J. Sound Vib. Vol. 265, No. 1 (2003), 201–219. DOI: 10.1016/S0022-460X(02)01447-5. oai : hal-01635272.

[21] T. M. Cameron and J. H. Griffin. An Alternating Frequency/Time Domain Method for Calculating the Steady-State Response of Nonlinear Dynamic Systems. J. Appl. Mech. Vol. 56, No. 1 (1989), 149–154. DOI: 10.1115/1.3176036. oai : hal-01333697.

[22] D. Charleux, C. Gibert, F. Thouverez, and J. Dupeux. Numerical and Experimental Study of Friction Damping Blade Attachments of Rotating Bladed Disks. Int. J. Rotating Mach. Vol. 2006 (2006), 1–13. DOI: 10.1155/IJRM/2006/71302.

[23] L. Salles, A. M. Gouskov, L. Blanc, F. Thouverez, and P. Jean. Dynamic Analysis of Fretting-Wear in Joint Interface by a Multiscale Harmonic Balance Method Coupled With Explicit or Implicit Integration Schemes. *Volume 6: Structures and Dynamics, Parts A and B*. Glasgow, UK, 2010, pp. 1003–1013. DOI: 10.1115/GT2010-23264. oai : hal-02529258.

[24] G. Von Groll and D. Ewins. The harmonic balance method with arc-length continuation in rotor/stator contact problems. J. Sound Vib. Vol. 241, No. 2 (2001), 223–233. DOI: 10.1006/jsvi.2000.3298. oai : hal-01333704.

[25] L. Woiwode, N. N. Balaji, J. Kappauf, F. Tubita, L. Guillot, C. Vergez, B. Cochelin, A. Grolet, and M. Krack. Comparison of two algorithms for Harmonic Balance and path continuation. Mech. Syst. Sig. Process. Vol. 136 (2020), 106503. DOI: 10.1016/j.ymssp.2019.106503. oai : hal-02424746.

[26] D. C. Urasek and W. T. Gorrell. Performance of two-stage fan having low-aspect-ratio first-stage rotor blading (1979), 132.

[27] H. Doi and J. J. Alonso. Fluid/Structure Coupled Aeroelastic Computations for Transonic Flows in Turbomachinery. *Proceedings of the ASME Turbo Expo 2002*. Vol. 4: Turbo Expo 2002, Parts A and B. Amsterdam, The Netherlands, 2002, pp. 787–794. DOI: 10.1115/GT2002-30313.

[28] Y. Colaïtis. Stratégie numérique pour l'analyse qualitative des interactions aube/carter. PhD thesis. École Polytechnique Montréal, 2021. tel-03318777.

[29] R. R. Craig and M. C. C. Bampton. Coupling of substructures for dynamic analyses. AIAA Journal Vol. 6, No. 7 (1968), 1313–1319. DOI: 10.2514/3.4741. oai : hal-01537654.

[30] D. Laity. *Stage 67 rotor and stage 67 casing half stators mounted. Records of the National Aeronautics and Space Administration*. 1980.

[31] A. Millecamps, J.-F. Brunel, P. Dufrénoy, F. Garcin, and M. Nucci. Influence of Thermal Effects During Blade-Casing Contact Experiments. *Proceedings of the ASME 2009 International Design Engineering Technical Conferences and Computers and Information in Engineering Conference*. Vol. 1: 22nd Biennial Conference on Mechanical Vibration and Noise, Parts A and B. San Diego, California, USA, 2009, pp. 855–862. DOI: 10.1115/DETC2009-86842. oai : hal-01223060.

[32] M. Krack and J. Gross. Harmonic Balance for Nonlinear Vibration Problems. Mathematical Engineering. Cham, 2019. DOI: 10.1007/978-3-030-14023-6.

[33] A. Grolet and F. Thouverez. Computing multiple periodic solutions of nonlinear vibration problems using the harmonic balance method and Groebner bases. Mech. Syst. Sig. Process. Vol. 52-53 (2015), 529–547. DOI: 10.1016/j.ymssp.2014.07.015. oai : hal-02121532.

[34] M. Volvert and G. Kerschen. Phase resonance nonlinear modes of mechanical systems. J. Sound Vib. Vol. 511 (2021), 116355. DOI: 10.1016/j.jsv.2021.116355.